A scintillating fiber imaging spectrometer for active characterisation of laser-driven proton beams - Supplementary material

J. K. Patel[1,2], C. D. Armstrong[2], R. Wilson[1], M. Alderton[1], E. J. Dolier[1], T. P. Frazer[1], A. Horne[1], A. Lofrese[1], M. Peat[1], M. Woodward[2], B. Zielbauer[3], R. J. Clarke[2], R. Deas[4], P. P. Rajeev[2], R. J. Gray[1], and P. McKenna[1,5]

[1]*SUPA Department of Physics, University of Strathclyde, Glasgow, G4 0NG, UK*

[2]*Central Laser Facility, STFC Rutherford Appleton Laboratory, Harwell, Oxford, OX11 0QX, UK*

[3]*PHELIX Group, GSI Helmholtzzentrum für Schwerionenforschung, Darmstadt, D-64291, Germany*

[4]*Defence Science and Technology Laboratory, Fort Halstead, Kent, TN14 7BS, UK*

[5]*The Cockroft Institute, Sci-Tech Daresbury, Warrington, WA4 4AD, UK*

1. Lens collection efficiency

Lacking an analytical model for emission at large angles, the dependence on numerical aperture used in Section 2.1 is obtained by a sigmoidal fit to measurements in Reference[1] for 1 mm diameter single-clad optical fibers, which are also used in the prototype presented in Section 2.2. Fitting

$$\varepsilon_{\text{lens}}(NA) = \exp\left(-A\exp\left(B - C\sin^{-1}(NA)\right)\right) \quad (1)$$

yields $A = 0.103, B = 6.41, C = 4.69$, with $R^2 = 0.999$.

For angles $\theta \leq 20° (= \pi/9$ rad), the angular distribution of emission from round, single-clad optical fibers increases linearly with polar angle[1,2], and the total fraction emitted into this cone is $\approx 1/4$. In the experimental cases presented in Sections 3.1 and 3.2 the half angle of the collecting lens is $<5°$, so the radiant intensity (flux per solid angle) is approximately

$$I_\Omega(\theta) = m\theta, \quad (2)$$

where m is found from the integral over polar and azimuthal angles,

$$m\int_0^{2\pi}\int_0^{\pi/9} \theta \, d\theta d\phi = \frac{1}{4}, \quad (3)$$

$$m = \frac{81}{4\pi^3}. \quad (4)$$

Equation (2) then becomes

$$I_\Omega(\theta) = \frac{81}{4\pi^3}\theta, \quad (5)$$

Correspondence to: jesel.patel@strath.ac.uk

and by assuming the collection lens is centred on the fiber optical axis, the lens collection efficiency is the integral over azimuthal $(0 < \phi < 2\pi)$, and polar angles $(0 < \theta < NA)$,

$$\varepsilon_{\text{lens}} = \int_0^{2\pi}\int_0^{NA} I_\Omega(\theta)d\theta d\phi, \quad (6)$$

$$\varepsilon_{\text{lens}} = \frac{81}{4\pi^2}NA^2, \quad (7)$$

where $NA = \tan^{-1}(d_{\text{lens}}/2d_{\text{W}})$ is the numerical aperture (equivalent to the half-angle subtended by the collection lens in the paraxial approximation) with lens diameter d_{lens}, and working distance d_{W}.

2. Flat-field calibration, fiber indexing and optical cross-talk

Ionising radiation induces emission of the scintillating fibers with a primary peak at 530 nm. This emission can also be induced by UV excitation, providing a useful route to characterising the fibers in a table-top setup with reduced safety requirements compared to more hazardous ionising radiation sources. Illuminating each scintillating fiber with a UV LED allowed indexing of each of the signals to an associated position in the image. By exciting an individual fiber, the optical cross-talk in all neighbouring fibers was measured to be $< 10^{-3}$ times the signal in the illuminated fiber. Relative variation in the fiber optical couplings mean that a flat field calibration is required. This was performed with a UV LED and a diffusing screen to homogenise the UV illumination, as illustrated in Figure 1a). The raw image and relative fiber signals from such a calibration are shown
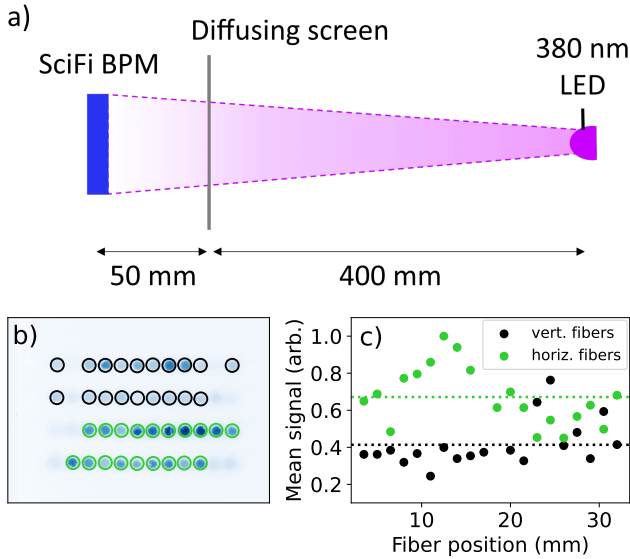
Figure 1 : Flat-field calibration of scintillating fibers using a UV LED. **a)** Setup schematic. **b)** False color flat field image of optical fiber ends. Black and green circles indicate fibers which are coupled to vertical and horizontal oriented scintillating fibers, respectively. **c)** Relative fiber signals sorted by position in array.

in Figures 1b) and c), respectively. This method was used for the results presented in Section 3 of the main text.

3. Particle analysis at $\sim$1/20 Hz

A second experiment used the SciFi BPM to diagnose the species and energy distribution of laser accelerated particles by spatially resolving differently filtered regions, while operating at $\sim$1/20 Hz repetition-rates. A series of single-shot measurements with the SciFi BPM were taken using fixed laser and target parameters, which were then averaged to increase the signal-to-noise ratio in the measured profiles. Measurements were made using the 350 TW SCAPA[3] laser in the solid target experimental area referred to as Bunker B, using the arrangement shown in Figure 2a). This was done during the commissioning of a new target station and so the laser parameters, such as energy and focal spot, as well as target thickness and pre-plasma scale length were not optimised for proton acceleration, but were sufficient to produce energetic particles suitable for testing the diagnostic. A $\tau_{\mathrm{L}} = (29.6 \pm 0.4)$ fs, $\lambda = 800$ nm laser pulse was incident to a 25 μm thick Kapton tape target at 10° with respect to the target normal axis. An $f/1.6$ off-axis parabola was used to produce focal spots with diameter $d = (3.2 \pm 0.4)$ μm FWHM, containing $E_{\mathrm{L}} = (133 \pm 4)$ mJ within the FWHM, resulting in an average peak intensity of $I_{\mathrm{L}} = (6 \pm 1) \times 10^{19}$ Wcm^{-2}. Uncertainties in the pulse duration and focal spot radius are based on frequency resolved optical gating (FROG) and focal spot imaging measurements, respectively. The encircled laser energy is based on the focal spot diameter measurements and calorimeter measurements averaged over

the 15 shots used in this work. A Thomson parabola spectrometer was positioned to measure the energy spectrum of ions along the laser axis. The SciFi BPM was positioned 630 mm from the laser focus, at polar and azimuthal angles $\theta = 15°$ and $\phi = 36°$ from target normal, respectively. For an initial run of 5 shots, 13 μm thick Al filtering was placed in front of the fibers to obtain an average beam profile. This measurement includes contributions to non-uniformity due to both the beam profile, and variation in the relative fiber throughput. In the absence of a calibration with a UV LED, this measurement can be used as a 'flat-frame' calibration to isolate the effect of introducing additional filtering. For a subsequent run of 10 shots, 300 μm Mylar and 3 mm Pb filtering was added to the lower two- and one-thirds of the front of the SciFi BPM, respectively, allowing particles to be resolved based on their minimum energy or species. Scintillating fibers were coupled at both ends to 2 m long optical transport fibers in this case, and the transport fibers were imaged with an $f/0.95$ lens at a working distance of $d_{\mathrm{W}} \approx 0.2$ m, resulting in a lens collection efficiency of 0.5%. An AVT Manta G-040B camera[4] with a Sony IMX287 CMOS sensor was used in this setup. A shorter working distance was chosen due to the expected reduction in fluence of accelerated particles due to lower laser energy and the greater distance of the SciFi BPM from the source compared to the setup in Section 3 of the main article, leading to lower scintillation light yield. Owing to the 7.2× increase in collection efficiency compared to the long working distance setup in Section 3 of the main article, and a 4.2× increase in the magnification of the imaging system, the energies deposited in a scintillating fiber to which this setup is sensitive are $\sim$30× smaller, at 160 MeV - 7.6 TeV, or 2.6 Gy - 120 kGy absorbed dose.

Imaging scintillation light from both ends of the fibers increases the collected signal, and therefore the signal-to-noise ratio in a single profile. Furthermore, attenuation of light due to transport losses in the scintillating fibers enables additional spatial information to be inferred. The ratio of the signals measured at each end of a scintillating fiber can be used to calculate the weighted average position of the scintillation emission along the length of the fiber. This is equivalent to measuring the first moment of the distribution of the scintillation emission as a 1D function of position along the length of the fiber, and is analogous to the center-of-mass of a mass distribution.

Figure 2b) illustrates the filtering in the second run of shots, and shows the average profiles obtained with the additional Pb and Mylar filtering, calibrated using the average flat-frame profile obtained from the shots with uniform Al filtering only. Positions of the plots (left, right, top, bottom) correspond to the ends of the scintillating fibers from which signals are transported by optical fibers. The additional Pb and Mylar filtering stops more protons in the lower portions of the beam, with significantly higher flux in
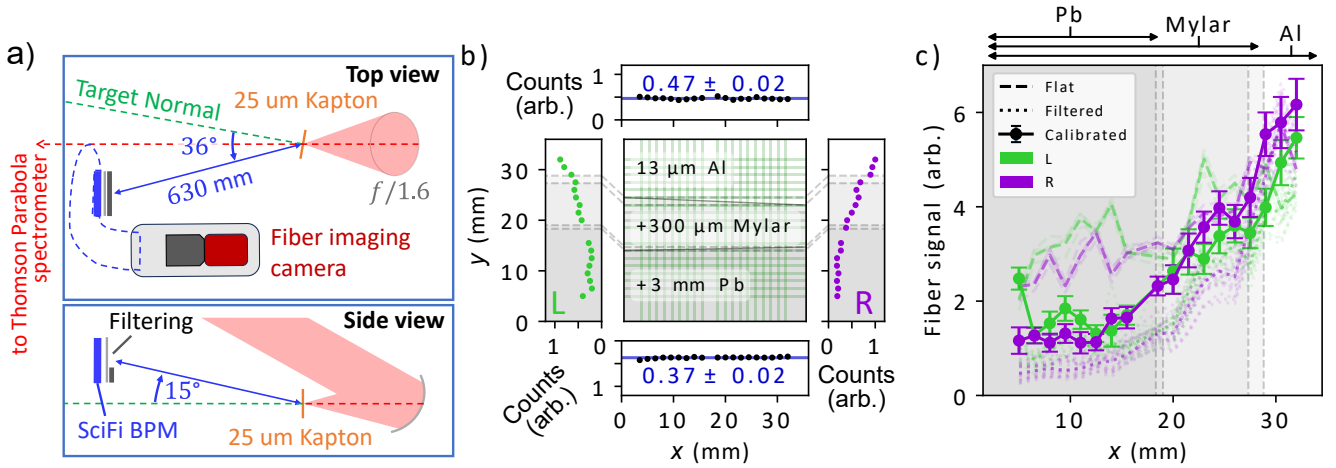
Figure 2 : a) Top and side views of experimental arrangement (not to scale) for high repetition particle discrimination measurements. **b)** Filter positions on front of SciFi BPM, illustration of fiber positions (light green rectangles) and plots of the processed mean signals. **b - Center)** Dashed grey lines indicate the position of filter edges. **b - Top & Bottom)** Blue lines and annotations are the mean of the signals from top and bottom coupled vertical scintillating fibers, with the standard deviations given as the errors. **b - Left & Right)** Dashed grey lines are the filter edges positions projected to the detection plane (see main text for details). White regions are filtered by Al only, light grey shaded regions are filtered by Al and Mylar, and darker grey shaded regions are filtered by Al, Mylar and Pb. **c)** Flat calibration profiles for 5 shots (dashed lines) and filtered profiles for 10 shots (dotted lines), with their respective mean profiles shown with darker colours. Solid lines and round symbols show the filtered profile calibrated by dividing by the normalised flat profile. See main text for error bar calculation. Signals from fibers coupled at the left and right ends are shown in green and purple, respectively. Black arrows and annotations indicate the extent of filter materials and shaded regions also indicate filtering as in **b)**.

the upper portion of the beam incident to the SciFi BPM. This is evident in the left (green) and right (purple) vertical profiles from the horizontal fibers. With higher proton flux generating more scintillation emission towards the top of the vertical fibers, the scintillation light undergoes less optical attenuation on average along the path to the top ends of the fibers than the bottom ends. This results in the higher average signal measured from the top ends of vertical fibers than the bottom ends, as annotated in blue on the horizontal profiles (top and bottom plots) in Figure 2b).

To verify that the relative difference in the signals in the top and bottom horizontal profiles is consistent with the measured vertical profiles, we can model the beam profile incident to the full length of the vertical fibers using the measured right-hand vertical profile. The measured vertical profile lacks data at positions $y < 5$ mm and $y > 32$ mm. With uniform filtering in these regions, we can assume the flat-field calibrated profile is constant here to model the beam profile incident to the full 36 mm length of the vertical fibers exposed to the beam. We therefore set the values at positions $y < 5$ mm and $y > 32$ mm in our modelled profile equal to the first and last respective samples in the measured vertical profile. The signal-weighted average of the positions in the resultant modelled vertical profile is $\langle y \rangle_{\text{vert.}} = 29$ mm. Fiber losses due to scintillation emission at angles greater than the fiber critical angle are independent of position in the fiber, and the bending radius of fibers is kept to $\gtrsim 60$ mm with the fiber clamps, causing losses $\lesssim 1\%$ [5]. These effects can thus be neglected. Attenuation due to scattering and absorption in the fiber material results in optical signals

decaying exponentially as a function of path length in the fiber, according to the Beer-Lambert law [6]. For a known length of fiber, L, the distance from the bottom of a fiber to the centre of mass of the optical emission in the fiber is

$$\langle y \rangle_{\text{atten.}} = \frac{L}{\ln\left(\frac{I_B}{I_A}\right) + 1}, \tag{8}$$

where I_B/I_A is the ratio of the signal measured at fiber end B to the signal at end A. Using the average relative signals from the bottom (A) and top (B) of vertical fibers, $I_B = (0.37 \pm 0.02)$, $I_A = (0.47 \pm 0.02)$, Equation (8) gives the average signal position, $\langle y \rangle_{\text{atten.}} = (29 \pm 2)$ mm, in close agreement with average position in the padded vertical profile.

Light green shaded regions in the middle panel of Figure 2b) show the positions of the scintillating fibers behind the filtering, and the solid grey lines are the edges of the filters. Dashed grey lines in Figures 2b) and 2c) show the maximum and minimum vertical positions of the filter edges in the vertical profiles, arising from small rotations of the filter edges from horizontal, measured as 1.1° and -2.4° for the Pb and Mylar filters, respectively. The position of the filter edges is projected to the plane of the scintillating fibers, which are 16 mm behind the filters, accounting for the 15° polar angle from the plane of the laser axis and target normal. Figure 2c) shows the profiles from the horizontal scintillating fibers read out from the left and right. Normalised profiles from the flat-field shots are shown with faint dotted lines, and those from the shots with the additional Pb and Mylar

filtering are shown with faint dashed lines. Darker dashed and dotted lines show the mean of the flat-field and the filtered profiles, respectively. The average filtered profiles calibrated with the average flat-field profiles are shown with solid lines and circle markers, and the error-bars are given by $\sqrt{\sigma_{\mathrm{flat}}^2 + \sigma_{\mathrm{filt}}^2}$, where σ_{flat} and σ_{filt} are the standard deviations of the flat and filtered signals, respectively.

Measurements made using a Thomson parabola ion spectrometer shown in Figure 3a) indicate maximum proton energies of $E_{\mathrm{max}} = 2.1$ MeV. It is found from Monte-Carlo simulations that all protons with energies up to this cutoff are stopped in the 300 μm Mylar and the 3 mm Pb filtering, and $\gtrsim 0.9$ MeV protons pass through the region with only 13 μm Al filtering. However, the measured profiles still have significant signal in the region with Mylar filtering, and the three regions are separated by relatively shallow gradient transitions, rather than a single sharp step.

Geant4[7] simulations have been conducted to investigate the effect of contributions from both protons and hot electrons on the vertical profiles. Expected contributions by x-ray was found to be negligible. Scintillating fibers are modelled as 500 μm diameter polystyrene cylinders, and the 13 μm Al, 300 μm Mylar and 3 mm Pb filters are included, accounting for the offsets and rotations of the filter edges, and the 15° projection over the 16 mm separation between the fibers and the filtering in the experimental geometry. A Maxwell-Boltzmann distribution is used to model the electron beam energy spectrum incident to the detector, with a $k_{\mathrm{B}}T_{\mathrm{e}} = 1.4$ MeV temperature taken from the ponderomotive scaling of electron temperature with laser

intensity[8]. The proton beam energy spectrum, $f_{\mathrm{p}}(E)$, is modelled with an energy distribution given by Equation (4) of the main article, using the hot electron temperature, $k_{\mathrm{B}}T_{\mathrm{e}} = 1.4$ MeV, a lower threshold of 0.5 MeV, a cutoff energy $E_{\mathrm{max}} = 2.1$ MeV, and calculating the normalised acceleration time, t_{p}, in accordance with Reference[9]. This modeled proton energy spectrum is shown with a red line in 3a), overlaid on proton spectra measured on 15 shots with the Thomson parabola (grey lines) and the mean of these 15 shots (black line). The modelled spectrum is normalised to the mean TP spectrum at $E = 0.5$ MeV. The SciFi BPM was not simultaneously run on these shots, but the same laser and target parameters were used to enable comparison.

Figure 3b) shows the normalised response of the scintillating fibers to the simulated electron and proton beams with blue and red lines, respectively. The relative responses are calculated as

$$R(x) = \frac{E_{\mathrm{dep}}(x)\kappa_{\mathrm{scint.}}\varepsilon_{\mathrm{opt.}}}{E_{\mathrm{tot.}}Q_{\mathrm{F}}}, \tag{9}$$

where E_{dep} is the energy deposited in the fibers and $E_{\mathrm{tot.}}$ is the total kinetic energy in each beam. For the simulated electron energies, the average LET in the fibers is $\lesssim 0.5$ MeVmm^{-1}, and so the quenching effect is relatively small ($\sim 5\%$) and we can make the approximation $Q_{\mathrm{F,e}} \approx 1$. Lower proton energies are generated in these lower laser energy, shorter pulse duration interactions compared to the measurements in Section 3 of the main article. Monte-Carlo simulations show that these lower energy protons have a greater path-averaged LET in the scintillator, resulting in a
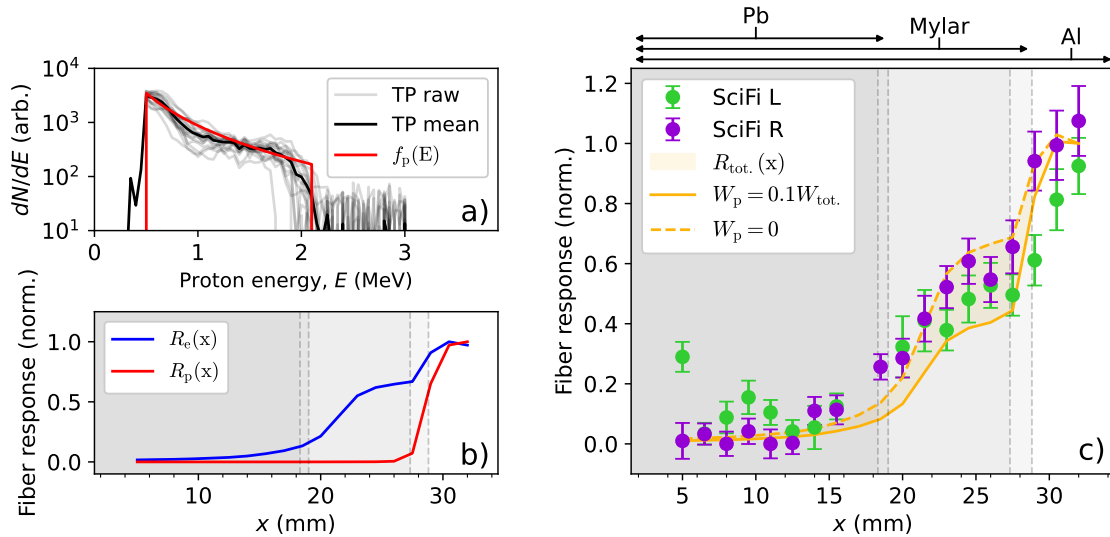

Figure 3 : **a)** Proton energy spectra measured using a Thomson parabola (TP) ion spectrometer on 15 shots (grey lines) using the same laser and target parameters and their mean (black line). Data above 3 MeV are all in the noise, and are truncated for clarity. The proton energy spectrum used for Geant4 simulations is shown with a solid red line. **b)** Normalised scintillating fiber response to the simulated electron beam (blue line) and proton beam (red line). **c)** Mean experimental profiles from fiber signals (green and purple) with combined profiles from simulations with electrons and protons (yellow), normalised to the average measured signals at $x = 32$ mm. The dashed yellow line shows the profile with no contribution by protons, and the solid yellow line shows the profile from combining the responses according to Equation (10) with a proton weight $W_{\mathrm{p}} = 0.1W_{\mathrm{tot.}}$.

higher $Q_{F,p} = 2.4$. Figure 3c) shows the measured vertical profiles with green and purple markers as in Figure 2c), along with combined fiber responses from the Monte-Carlo simulations. Contributions to the total detector response by electrons and protons can be combined as in Equation (10),

$$R_{tot.}(x) = \frac{(W_{tot.} - W_p)R_e(x) + W_p R_p(x)}{W_{tot.}}, \quad (10)$$

where $R_e(x)$ and $R_p(x)$ are the electron and proton responses calculated with Equation (10) using $Q_{F,e}$ and $Q_{F,p}$ respectively, $W_{tot.}$ is the total beam flux and W_p is the proton flux. The dashed yellow line in Figure 3c) shows the combined profile with $W_p = 0$, i.e. with no contribution by protons. The solid yellow line shows the profile with $W_p = 0.1W_{tot.}$, corresponding to a 10% contribution by protons to the total beam flux. Each of these profiles is normalised to the signal in the final fiber, at position $x = 32$ mm, so that the shapes of the two profiles can be compared with respect to the measured data. The region between the the two cases is shaded yellow to indicate the range of values for W_p which are in agreement with the measured profiles. With the strongest deposition by protons in the region with Al filtering only, the relative signal in the other regions is reduced when the contribution by protons is increased to $W_p = 0.1W_{tot.}$. When W_p is increased further, the modelled response in the regions with additional Mylar and Pb filtering is significantly lower than the measured data. Based on this analysis, at the resultant polar and azimuthal angle of 39° of the SciFi BPM from target normal, the protons contribute a maximum of 10% to the total beam flux.

References

1. S. Nieswand. *Measurement of the exit characteristics of light from optical multimode plastic fibres*. PhD thesis, RWTH Aachen U., 2014. URL https://cds.cern.ch/record/2285971.

2. T. Bretz, R. Engel, T. Hebbeker, J. Kemp, L. Middendorf, C. Peters, J. Schumacher, R. Šmìda, and D. Veberič. An integrated general purpose SiPM based optical module with a high dynamic range. *Journal of Instrumentation*, 13(06):P06001, Jun 2018. URL https://dx.doi.org/10.1088/1748-0221/13/06/P06001.

3. S. M. Wiggins, M. Boyd, E. Brunetti, N. M. H. Butler, J. S. Feehan, R. J. Gray, B. Hidding, D. G. Ireland, W. Li, A Maitrallain, G. G. Manahan, P. McKenna, D. O'Donnell, M. Scheck, M. Shahzad, Z.-M. Sheng, R. Spesyvtsev, G. Vieux, D. P. Watts, G. H. Welsh, R. Wilson, N. Zachariou, and D. A. Jaroszynski. Application programmes at the Scottish Centre for the Application of Plasma-based Accelerators (SCAPA). *Proceedings of SPIE 11036: Relativistic Plasma Waves and Particle Beams as Coherent and Incoherent Radiation Sources III*, page 110360T, Apr 2019. URL https://doi.org/10.1117/12.2520717.

4. Allied Vision Technologies GmbH. Modular machine vision camera with GigE Vision interface. URL https://www.alliedvision.com/en/camera-selector/detail/manta/g-040/. Last accessed 24 June 2024.

5. Kuraray Co. Ltd. Plastic scintillating fibers. URL https://www.kuraray.com/products/psf. Last accessed 4 December 2023.

6. Beer. Bestimmung der absorption des rothen lichts in farbigen flüssigkeiten. *Annalen der Physik*, 162 (5):78–88, 1852. URL https://doi.org/10.1002/andp.18521620505.

7. S. Agostinelli, J. Allison, K. Amako, J. Apostolakis, H. Araujo, P. Arce, M. Asai, D. Axen, S. Banerjee, G. Barrand, F. Behner, L. Bellagamba, J. Boudreau, L. Broglia, A. Brunengo, H. Burkhardt, S. Chauvie, J. Chuma, R. Chytracek, G. Cooperman, G. Cosmo, P. Degtyarenko, A. Dell'Acqua, G. Depaola, D. Dietrich, R. Enami, A. Feliciello, C. Ferguson, H. Fesefeldt, G. Folger, F. Foppiano, A. Forti, S. Garelli, S. Giani, R. Giannitrapani, D. Gibin, J. J. Gómez Cadenas, I. González, G. Gracia Abril, G. Greeniaus, W. Greiner, V. Grichine, A. Grossheim, S. Guatelli, P. Gumplinger, R. Hamatsu, K. Hashimoto, H. Hasui, A. Heikkinen, A. Howard, V. Ivanchenko, A. Johnson, F. W. Jones, J. Kallenbach, N. Kanaya, M. Kawabata, Y. Kawabata, M. Kawaguti, S. Kelner, P. Kent, A. Kimura, T. Kodama, R. Kokoulin, M. Kossov, H. Kurashige, E. Lamanna, T. Lampén, V. Lara, V. Lefebure, F. Lei, M. Liendl, W. Lockman, F. Longo, S. Magni, M. Maire, E. Medernach, K. Minamimoto, P. Mora de Freitas, Y. Morita, K. Murakami, M. Nagamatu, R. Nartallo, P. Nieminen, T. Nishimura, K. Ohtsubo, M. Okamura, S. O'Neale, Y. Oohata, K. Paech, J. Perl, A. Pfeiffer, M .G. Pia, F. Ranjard, A. Rybin, S. Sadilov, E. Di Salvo, G. Santin, T. Sasaki, N. Savvas, Y. Sawada, S. Scherer, S. Sei, V. Sirotenko, D. Smith, N. Starkov, H. Stoecker, J. Sulkimo, M. Takahata, S. Tanaka, E. Tcherniaev, E. Safai Tehrani, M. Tropeano, P. Truscott, H. Uno, L. Urban, P. Urban, M. Verderi, A. Walkden, W. Wander, H. Weber, J. P. Wellisch, T. Wenaus, D. C. Williams, D. Wright, T. Yamada, H. Yoshida, and D. Zschiesche. Geant4 — a simulation toolkit. *Nuclear Instruments and Methods in Physics Research Section A: Accelerators, Spectrometers, Detectors and Associated Equipment*, 506(3):250–303, 2003. URL https://doi.org/10.1016/S0168-9002(03)01368-8.

8. S. C. Wilks, W. L. Kruer, M. Tabak, and A. B. Langdon. Absorption of ultra-intense laser pulses. *Phys. Rev. Lett.*, 69:1383–1386, Aug 1992. URL https://doi.org/10.1103/PhysRevLett.69.1383.

9. J. Fuchs, P. Antici, E. d'Humières, E. Lefebvre, M. Borghesi, E. Brambrink, C. A. Cecchetti, M. Kaluza, V. Malka, M. Manclossi, S. Meyroneinc, P. Mora, J. Schreiber, T. Toncian, H. Pépin, and P. Audebert. Laser-

driven proton scaling laws and new paths towards energy increase. *Nature Physics*, 2(1):48–54, Dec 2006. URL https://doi.org/10.1038/nphys199.